NASA TM-86432

NASA Technical Memorandum 86432

NASA-TM-86432 19850021619

UNSTEADY TRANSONIC FLOW CALCULATIONS FOR INTERFERING LIFTING SURFACE CONFIGURATIONS

JOHN T. BATINA

MAY 1985

National Aeronautics and
Space Administration

Langley Research Center
Hampton, Virginia 23665

UNSTEADY TRANSONIC FLOW CALCULATIONS FOR INTERFERING LIFTING SURFACE CONFIGURATIONS

John T. Batina
NASA Langley Research Center
Hampton, Virginia 23665

Abstract

Unsteady transonic flow calculations are presented for aerodynamically interfering lifting surface configurations. Calculations are performed by extending the XTRAN3S (Version 1.5) unsteady transonic small-disturbance code to allow the treatment of an additional lifting surface. The research was conducted as a first-step toward developing the capability to treat a complete flight vehicle. Grid generation procedures for swept tapered interfering lifting surface applications of XTRAN3S are described. Transonic calculations are presented for wing-tail and canard-wing configurations for several values of mean angle of attack. The effects of aerodynamic interference on transonic steady pressure distributions and steady and oscillatory spanwise lift distributions are demonstrated. Results due to wing, tail, or canard pitching motions are presented and discussed in detail.

Nomenclature

c	airfoil chord
c_ℓ	sectional lift coefficient
c_r	wing reference chord
f	function defining instantaneous position of lifting surface
k	reduced frequency, $\omega c_r/2U$
M	freestream Mach number
S	horizontal separation distance measured in wing root chordlength between the two planform root sections
t	time nondimensionalized by freestream velocity and wing reference chord
U	freestream velocity
x,y,z	nondimensional cartesian coordinates in streamwise, spanwise, and vertical directions, respectively
y_j	coordinate of jth spanwise gridpoint
α	angle of attack
γ	ratio of specific heats
ΔC_p	lifting pressure coefficient
Λ	sweep angle
$\bar{\eta}$	fractional semispan
ξ,η,ζ	transformed nondimensional coordinates in x, y, and z directions, respectively
φ	disturbance velocity potential
ω	angular frequency

Subscripts

C	canard
LE	leading edge
T	tail
TE	trailing edge
W	wing
o	mean value
1	dynamic value

Introduction

Computational methods employing linear theory for predicting unsteady flowfields about aerodynamically interfering lifting surfaces and multiple-component configurations have been developed over the past fifteen years (Refs. 1-4, for example). These methods are extensions of linearized theory for single lifting surfaces to more complicated configurations such as two lifting surfaces in tandem, various horizontal stabilizer/vertical fin arrangements, and wing-body combinations. More recently, computer programs such as that reported in Ref. 5 have been developed for the analysis of complete flight vehicles. The underlying linear theory on which these methods are based, though, restricts the applications to either subsonic or supersonic flows. In the transonic regime, computational methods for predicting flowfields about oscillating multiple lifting surface configurations are currently being developed.

Steady transonic flowfields about isolated wings have been calculated by Boppe[6] using a finite-difference relaxation scheme with a grid embedding procedure. The isolated wing formulation was extended to permit the analysis of two interfering wing surfaces. Steady pressure distributions were presented to illustrate canard-wing interference at transonic speeds. Shankar and Malmuth[7] presented computations for a few canard-wing configurations using transonic small-disturbance theory. In Ref. 7, results were obtained by placing the two surfaces in a single sheared fine grid system that is embedded in a global cartesian crude grid. Shankar and Goebel[8] developed a local numerical mapping procedure where the leading and trailing edges of the two surfaces are treated as constant coordinate lines in the computational domain. The computations have also recently been extended to include dihedral and fuselage effects.[9]

Unsteady transonic results for two-dimensional canard-wing configurations were reported by the author in Ref. 10. The aerodynamic calculations were performed by extending the XTRAN2L[11] transonic small-disturbance code to include an additional airfoil. Results for a range of canard-wing separation distances demonstrated the effects of aerodynamic interference on transonic unsteady airloads, aeroelastic stability, and flutter of oscillating airfoils.

This paper presents three-dimensional transonic unsteady aerodynamic results from the XTRAN3S[12] transonic small-disturbance (TSD) code for oscillating interfering lifting surface configurations. The objectives of the study were to: (1) develop and demonstrate an unsteady transonic computational capability for interfering lifting surface geometries; and (2)

investigate the effects of aerodynamic interference on transonic pressures and forces. In this study, the calculations are performed by extending the XTRAN3S code to allow the treatment of an additional lifting surface. The interfering lifting surface computational capability now permits the assessment of aerodynamic interference effects on transonic unsteady airloads and flutter characteristics of closely-coupled wing-tail and canard-wing systems.

Computational Procedures

In this section, the XTRAN3S code and coordinate transformation details are described. Grid generation procedures for interfering lifting surface applications are also given.

XTRAN3S Code

Program Description. - The XTRAN3S code provides a time-accurate solution to the nonlinear, small-disturbance, potential equation for three-dimensional transonic flow. The code can be used to calculate steady and unsteady transonic flowfields about isolated planar wings including aeroelastic deformation effects. The program is capable of treating either forced harmonic or aeroelastic transient type motions. A time-accurate alternating-direction implicit (ADI) finite-difference scheme is used to solve the modified transonic small-disturbance equation

$$M^2(\phi_t + 2\phi_x)_t = [(1 - M^2)\phi_x + A\phi_x^2 + B\phi_y^2]_x + (\phi_y + C\phi_x\phi_y)_y + (\phi_z)_z \quad (1)$$

Several choices are available for the coefficients A, B, and C, depending upon the assumptions used in deriving the TSD equation.[12] Briefly, the coefficients are referred to as "NASA Ames" coefficients when defined as

$$A = -\frac{1}{2}(\gamma + 1)M^2 \quad (2a)$$

$$B = \frac{1}{2}(\gamma - 3)M^2 \quad (2b)$$

$$C = -(\gamma - 1)M^2 \quad (2c)$$

and are referred to as "NLR" coefficients when defined as

$$A = -\frac{1}{2}[3-(2-\gamma)M^2]M^2 \quad (3a)$$

$$B = -\frac{1}{2}M^2 \quad (3b)$$

$$C = -M^2 \quad (3c)$$

The "classical" coefficients are given by

$$A = -\frac{1}{2}(\gamma+1)M^2 \quad (4a)$$

$$B = 0 \quad (4b)$$

$$C = 0 \quad (4c)$$

and finally the coefficients for the linear equation are

$$A = B = C = 0 \quad (5)$$

The subsonic flat plate results presented herein are computed using the linear equation coefficients; the transonic results are computed using the NASA Ames coefficients. For wing-tail and canard-wing applications, the ADI solution procedure of XTRAN3S has been extended to allow the treatment of an additional lifting surface. The modifications have been made to Version 1.5[13] of the XTRAN3S code. The program now is capable of computing unsteady transonic flowfields about relatively general interfering lifting surface configurations. The present program coding, however, does not allow for overlapping or co-planar configurations.

Boundary conditions imposed upon the flowfield are

Far upstream: $\phi = 0$ (6a)

Far downstream: $\phi_x + \phi_t = 0$ (6b)

Far above and below: $\phi_z = 0$ (6c)

Far spanwise: $\phi_y = 0$ (6d)

Root reflection plane: $\phi_y = 0$ (6e)

Trailing wakes: $[\phi_z] = 0$ (6f)

$[\phi_x + \phi_t] = 0$ (6g)

where [ ] indicates the jump in the indicated quantity across the wake. The flow tangency boundary condition is

$$\phi_z^{\pm} = f_x^{\pm} + f_t^{\pm} \quad (7)$$

which is applied on the respective mean planes of the lifting surfaces.

Coordinate Transformation. - The finite-difference grids in both the physical and computational domains are contained within rectangular regions and conform to the two lifting surfaces. Regions in the physical domain, such as the swept and/or tapered lifting surface planforms and their outboard extensions, are mapped into rectangular regions in the computational domain using the shearing transformation

$$\xi = \xi(x,y) \quad (8a)$$

$$\eta = y \quad (8b)$$

$$\zeta = z \quad (8c)$$

The coordinate transformation (Eqs. (8)) is based on the single surface transformation equations described in detail by Bennett, et al.[14] For interfering lifting surface configurations, the transformation is applied independently in five separate regions of the grid as illustrated in Fig. 1. The five regions

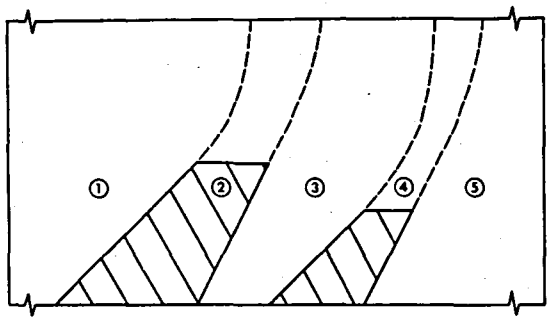

Fig. 1 Regions in physical domain which transform to rectangular regions in computational domain.

are defined as: (1) upstream of the "forward" planform; (2) along the forward planform and outboard extension; (3) between the two planforms; (4) along the "aft" planform and outboard extension; and (5) downstream of the aft planform.

Grid Generation Procedures

Sectional Grid Treatment. - The sectional finite-difference grid near a simple wing-tail configuration is shown in Fig. 2. Planar wakes are assumed for both lifting surfaces. The grid is based on the XTRAN3S isolated wing default grid described in Ref. 15 and has 93 and 46 points in the horizontal and vertical directions, respectively, for the configuration shown. Thirty equidistantly spaced points are distributed along both the wing and tail chords. One additional point is added near the leading edge of each surface for better resolution. Grid stretching to the farfield in both the x and z-directions is identical to that described in Ref. 15. In the streamwise direction, for example, gridpoints are stretched twenty chordlengths to the farfield with eleven and ten points extending to upstream and downstream boundaries, respectively. Above the tail and below the wing, twenty gridpoints are stretched twenty-five chordlengths to the upper and lower farfield boundaries. Between the two surfaces, vertical grid lines are distributed equidistantly between the first gridpoint downstream of the wing trailing edge and the tail leading edge. Horizontal grid lines are distributed equidistantly between the wing and tail centerlines with one additional line placed symmetrically below the tail centerline and another additional line placed symmetrically above the wing centerline. Horizontal and vertical separation distances are 50% and 40% chord, respectively, for the configuration shown here. For different separation distances or other configurations, points may be added or removed between the two lifting surfaces.

Planform Grid Treatment. - Figure 3 shows the planform finite-difference grid near a simple wing-tail configuration consisting of two identical swept planforms. The grid is based on the single surface grid mapping procedures described in Ref. 14 which were extended in this study to include an additional planform. A cosine distribution of spanwise gridpoints is used in this example along the lifting surfaces and in the outboard region to concentrate points near the tips. Outboard of the lifting surfaces, the planforms are extended to the farfield boundary using the outboard grid mapping procedure of Bennett, et al.[14] In this procedure, the leading and trailing edges are smoothly extended using cubic polynomials that match leading and trailing edge slopes and intersect the far spanwise boundary perpendicularly. The spanwise grid lines are mapped into the computational domain where they are treated as constant coordinate lines, similar to the local numerical mapping procedure of Ref. 8. Details of the grid mapping procedure and the equations defining the gridpoints are given in Ref. 14 for single lifting surface applications of XTRAN3S. Planform grids for the interfering lifting surface configurations presented below graphically illustrate the outboard grid mapping procedure.

In initial applications to both single and interfering lifting surface cases, numerical instability problems at the root were encountered. A representative example for a forward-swept wing configuration is shown in Fig. 4(a). Oscillations in the solution develop at the root as shown for t = 1.8 (120 time steps). These oscillations grow large with time and subsequently lead to program failure at t = 2.43 (162 time steps) for this example. A study was undertaken to investigate this instability

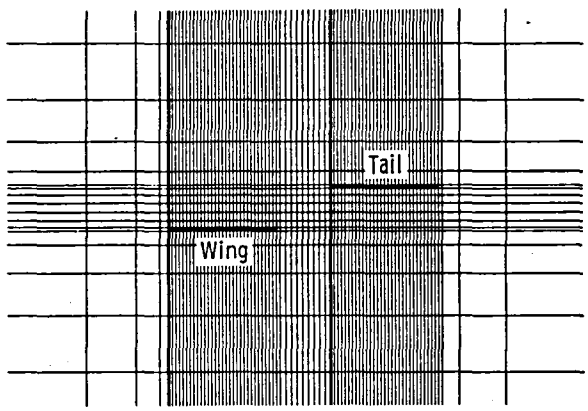

Fig. 2 XTRAN3S sectional finite-difference grid near wing-tail configuration of Ref. 4.

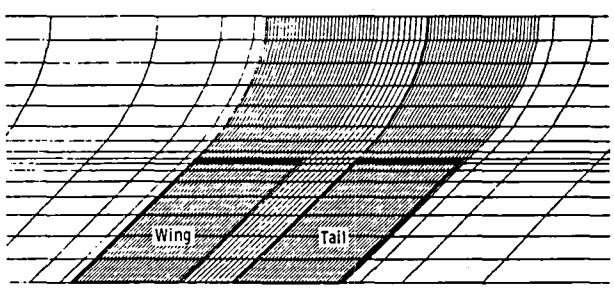

Fig. 3 XTRAN3S planform finite-difference grid near wing-tail configuration of Ref. 4.

and to seek solutions to eliminate the problem. The source of the instability was traced to the original treatment of the symmetry condition and grid near the root reflection plane for certain configurations and flow conditions. The symmetry condition (Eq. 6(e)) is expressed in the computational domain as

$$\phi_\xi \xi_y + \phi_\eta = 0 \qquad (9)$$

where ξ_y is the spanwise grid metric along the reflection plane. In XTRAN3S, a "dummy" plane adjacent to the reflection plane provides gridpoints for a central-difference approximation of ϕ_η in Eq. (9). The locations of these gridpoints in the original code are determined by extrapolating the grid lines in the physical domain across the reflection plane to the dummy plane as shown in Fig. 4(a). A new treatment of the grid was investigated such that these gridpoints are positioned symmetrically about the reflection plane as shown in the left part of Fig. 4(b). In this new grid treatment, the metric ξ_y is discontinuous across the reflection plane and is therefore not defined. Calculations are performed by setting ξ_y equal to zero, which is equivalent to taking an average of the values of ξ_y on either side of the reflection plane, and the symmetry condition becomes simply

$$\phi_\eta = 0 \qquad (10)$$

The new symmetric treatment of the grid eliminates the instability at the root and converged steady pressure results were obtained as shown in the right part of Fig. 4(b). For this forward-swept wing configuration, the program now predicts a steady pressure distribution with a relatively strong shock wave at the root. Moving outboard the shock weakens in strength and disappears toward the tip. Further investigation is required to assess the accuracy of these results.

The symmetric grid treatment can also be successfully applied to aft-swept configurations such as that presented in Fig. 4(c). The resulting steady presure distribution is smooth at the root and indicates the presence of a mild shock that is more pronounced at the tip. For highly-swept configurations, though, a non-physical pressure expansion may occur near the wing apex due to the sharp corner introduced by the symmetric grid. This nonphysical pressure expansion occurred for the configuration of

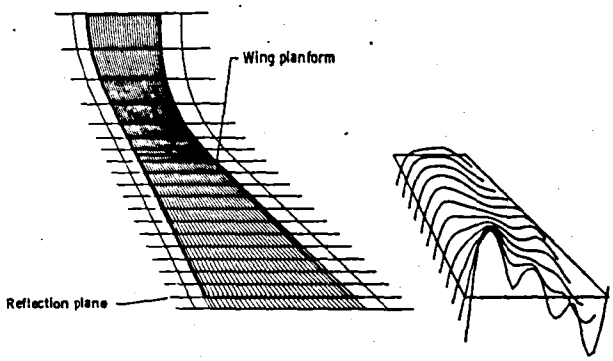

(a) original grid treatment at wing root for forward-swept wing and steady pressure distribution at t = 1.8.

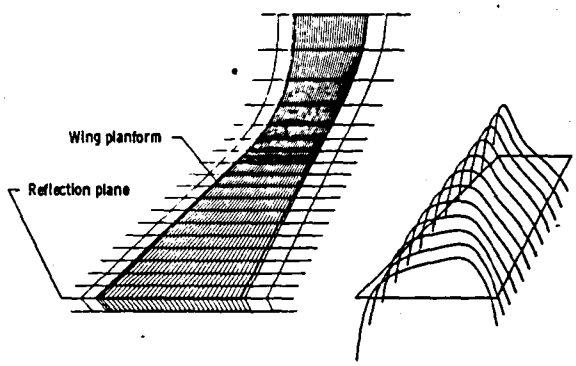

(c) symmetric grid treatment at wing root for aft-swept wing and steady pressure distribution at t = 24.0.

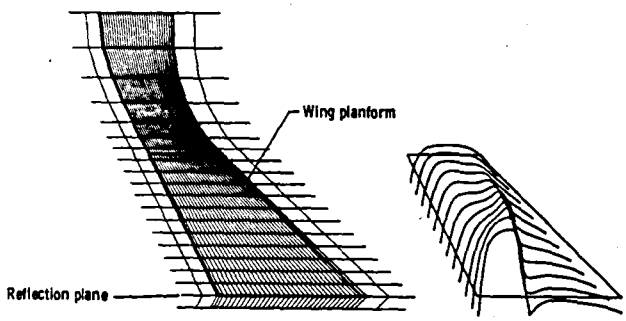

(b) symmetric grid treatment at wing root for forward-swept wing and steady pressure distribution at t = 24.0.

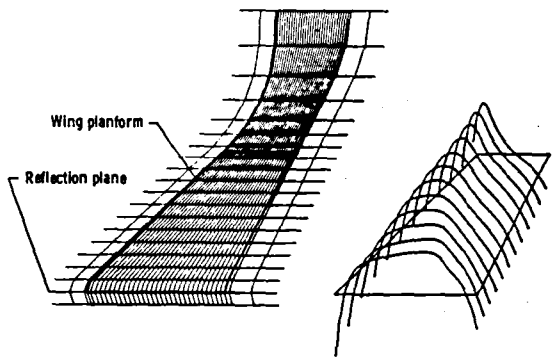

(d) symmetric grid treatment with parabolic smoothing at wing root and steady pressure distribution at t = 24.0.

Fig. 4 Treatment of planform grid across reflection plane and resulting steady pressure distributions at M = 0.9 and $\alpha_0 = 0^\circ$;

Fig. 4(c) when a cosine distribution of spanwise gridpoints was used. An inboard grid mapping procedure was subsequently developed to eliminate the corner by smoothing the grid across the reflection plane. In this procedure, the leading and trailing edges of the planforms near the root sections are replaced by second-order polynomials of the form

$$x_{LE}(y) = A_{LE}y^2 + B_{LE}y + C_{LE} \qquad (11a)$$

$$x_{TE}(y) = A_{TE}y^2 + B_{TE}y + C_{TE} \qquad (11b)$$

The coefficients in Eqs. (11) are determined by requiring that the polynomials intersect the reflection plane perpendicularly and match the locations and slopes of the leading and trailing edges at the first spanwise gridpoints outboard of the root section ($y = y_3$). The inboard grid mapping procedure with parabolic smoothing therefore replaces the leading and trailing edges at the root ($y = y_2 = 0$) by

$$x_{LE}(0) = x_{LE}(y_3) - \frac{1}{2} y_3 \tan^{-1}\left(\frac{\pi}{2} - \Lambda_{LE}\right) \qquad (12a)$$

$$x_{TE}(0) = x_{TE}(y_3) - \frac{1}{2} y_3 \tan^{-1}\left(\frac{\pi}{2} - \Lambda_{TE}\right) \qquad (12b)$$

which effectively unsweeps the grid near the reflection plane as shown in Fig. 4(d). This grid variation produces metrics ξ_y that are continuous and, along the reflection plane, are uniquely defined to be zero. The resulting steady pressure distribution using this grid treatment is also shown in Fig. 4(d). These steady pressures are smooth at the root and are similar to those shown in Fig. 4(c) (calculated using no smoothing along the root). A comparison of steady pressure distributions computed using three different grid variations is shown in Fig. 5 for the root section of the aft-swept wing. The symmetric treatment of the grid with parabolic smoothing produces a steady pressure distribution that is more forward loaded in comparison with the original and symmetric (without root smoothing) grids. This effect is attenuated in the spanwise direction and is negligible at the tip. Further work is needed to determine the accuracy of results computed using the symmetric grid with root smoothing by comparison with experiment.

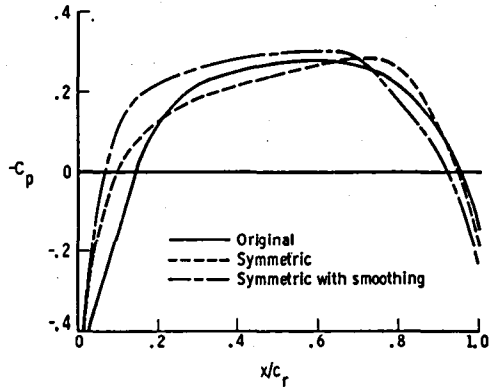

Fig. 5 Comparison of steady pressure distributions for aft-swept wing root section computed using three grid variations across reflection plane.

Planform finite-difference grids for the wing-tail and canard-wing configurations considered herein, are shown in Figs. 6(a) and 6(b), respectively. These grids clearly illustrate the inboard root smoothing and the outboard grid mapping procedures for interfering lifting surface configurations. The outboard grid mapping of Ref. 14 is applicable for most wing-tail and canard-wing configurations. For geometries consisting of a forward-swept wing with a closely-coupled aft-swept canard, however, the outboard extensions of the two planforms may overlap. The mapping has subsequently been modified to resolve this problem by simply altering the locations where the outboard extensions intersect the far spanwise boundary. The modification separates the two outboard extensions such that the overlap no longer occurs and reasonable planform grids for closely-coupled configurations may be obtained.

Results and Discussion

Configurations

Results are presented for the following three configurations: (1) a simple wing-tail consisting of two identical swept planforms; (2) the Laschka-Schmidt wing-tail[3]; and (3) a

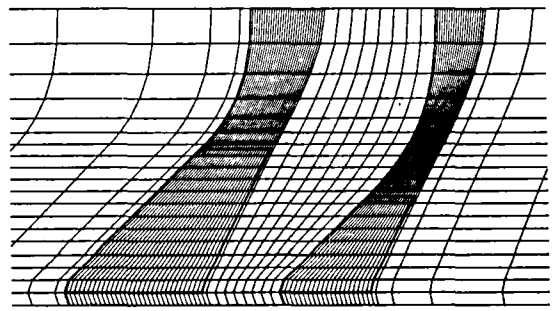

(a) Laschka-Schmidt wing-tail.

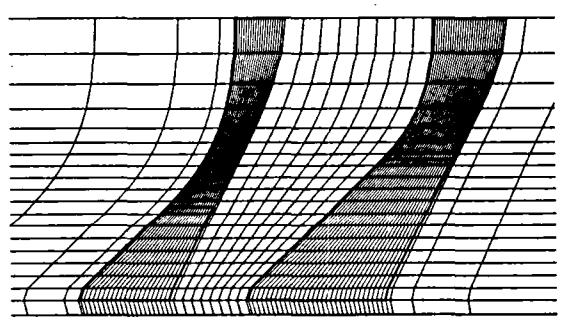

(b) canard-wing configuration.

Fig. 6 XTRAN3S planform finite-difference grids near interfering lifting surface configurations (S = 0.50);

canard-wing geometry. Subsonic unsteady calculations were performed for the first configuration for comparison with the linear theory results of Ref. 4. Transonic steady and unsteady results were obtained for the second and third configurations to demonstrate the XTRAN3S interfering lifting surface capability and to investigate the effects of aerodynamic interference on pressure distributions and spanwise loading.

Subsonic unsteady results are presented for the simple flat-plate wing-tail configuration illustrated in Figs. 2 and 3, to assess and verify the modifications to the XTRAN3S code. This configuration was selected for comparison with the linear theory results reported by Albano, Perkinson, and Rodden.[4] In Ref. 4, subsonic results were obtained for this configuration using a kernel function method. As illustrated in Fig. 3, each planform of the wing-tail has a full-span aspect ratio of 2.28, a leading edge sweep angle of 45°, and a taper ratio of 1.0.

Transonic steady and unsteady results are presented for the Laschka-Schmidt wing-tail and a canard-wing configuration. Each planform of these configurations has a full-span aspect ratio of 2.67, a leading edge sweep angle of 45°, and a taper ratio of 0.5. The tail of the Laschka-Schmidt configuration is two-thirds the size of the wing as illustrated by the planform finite-difference grid of Fig. 6(a). The canard-wing configuration is created by simply placing the tail in front of the wing as illustrated by the planform finite-difference grid of Fig. 6(b). The grids contain 82 x 20 x 44 points in the x, y, and z directions, respectively, for a total of 72,160 points. The vertical separation distance for the tail and canard was selected as 20% wing root chord above the wing. Two horizontal separation distances (between the planform root sections) of 25% (S = 0.25) and 50% (S = 0.50) wing root chord were considered. The NACA 0010 airfoil section was selected for the lifting surfaces. These similar wing-tail and canard-wing geometries were selected to study transonic interference effects because the lifting surfaces are all geometrically the same. Differences in pressure distributions or spanwise loading between the wing and the tail or between the canard and the wing are, therefore, due solely to aerodynamic interference.

Steady computations also were attempted for the Rockwell canard-wing model of Ref. 16. Each of the two lifting surfaces had an exposed aspect ratio of approximately 2.0, a leading edge sweep angle of approximately 40°, and a taper ratio slightly greater than 0.25. The wing also had 5° of parabolic twist washout. Attempts to obtain converged steady pressure distributions for both the canard-wing as well as for the isolated wing were unsuccessful due to a numerical instability that first was observed in the wing wake. The instability was attributed to the large twist of the low aspect ratio wing since steady solutions were obtainable for the wing with no twist.

Subsonic Linear Theory Comparison

Subsonic unsteady computations for the swept wing-tail configuration of Figs. 2 and 3 were performed for simple harmonic wing pitching about a line perpendicular to the root at the wing apex. The freestream Mach number was M = 0.7, the mean angle of attack was $\alpha_0 = 0°$ for both wing and tail, and the reduced frequency based on root semichord was k = 0.262. The nondimensional time step size was selected as $\Delta t = 0.01872$ which results in 640 time steps per cycle of motion.

Unsteady chordwise lifting pressure distributions ΔC_p on the wing and tail due to wing pitching with oscillation amplitude $\alpha_1 = 1°$ are shown in Fig. 7 for four span stations. Real and imaginary components of the lifting pressures are shown. These results were obtained using the symmetric treatment of the grid across the reflection plane without smoothing. The XTRAN3S results are in good general agreement with the kernel function method results of Ref. 4, with the largest differences occurring in the leading edge regions. Calculations performed using the original (extrapolated) treatment of the grid, however, did not predict the correct singular behavior near the leading edge of the root sections. This suggests that the symmetric grid treatment may be more applicable to unsteady calculations than the original grid treatment. The unsteady pressures on the motionless tail are induced by the oscillatory wing pitching motion and represent the unsteady aerodynamic interference of the wing on the tail. As discussed by Albano, et al.,[4] the upstream influence of the tail on the wing is negligible for this case.

Unsteady sectional lift coefficients on the wing and tail due to wing pitching are presented in Fig. 8. These coefficients are plotted as real and imaginary components of the spanwise lift distribution. As shown in Fig. 8, the XTRAN3S calculations agree very well with the linear theory results of Ref. 4. The unsteady lift coefficients on the tail induced by the wing pitching are similar in magnitude to the self-induced lift coefficients on the wing.

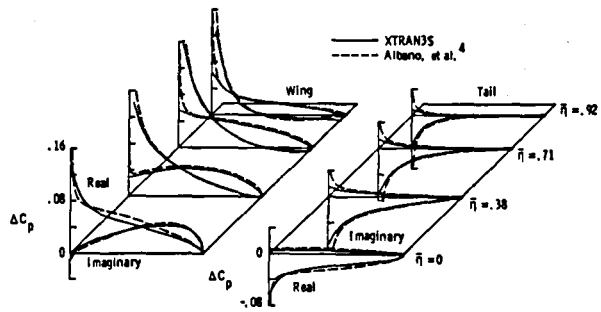

Fig. 7 Comparison between XTRAN3S and kernel function method unsteady chordwise lifting pressure distributions on wing and tail due to wing pitching at M = 0.7 and k = 0.262.

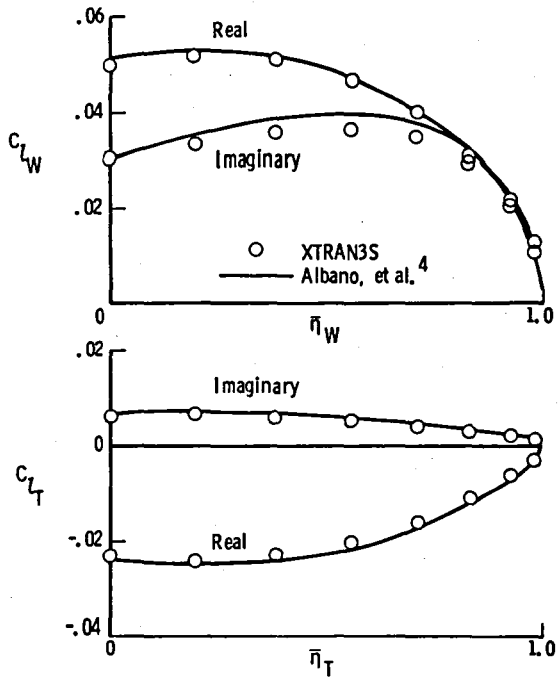

Fig. 8 Comparison between XTRAN3S and kernel function method unsteady sectional lift coefficients on wing and tail due to wing pitching at M = 0.7 and k = 0.262.

Transonic Steady Interference Effects

Transonic results for the Laschka-Schmidt wing-tail of Fig. 6(a) and the canard-wing configuration of Fig. 6(b) were obtained at a freestream Mach number of M = 0.9 and three mean angles of attack α_0 = 0°, 1°, and 2°. For steady calculations, the step size was selected as Δt = 0.015 and 1600 steps were required for the solution to converge.

Steady pressure distributions on the upper and lower surfaces of the isolated lifting surface at M = 0.9 and α_0 = 2° are shown in Figs. 9(a) and 9(b), respectively. These results are presented for comparison with the interfering lifting surface pressure distributions which follow. As shown in Fig. 9(a), there is a relatively strong shock wave on the upper surface located near 85% chord at the root. In the spanwise direction, the shock becomes more pronounced and is located near 30% chord at the tip. Although not obvious, the lower surface pressures shown in Fig. 9(b) are supercritical. Steady pressure distributions on the upper and lower surfaces of the wing-tail at M = 0.9 and α_0 = 2° are plotted in Figs. 10(a) and 10(b), respectively. In general, the pressures on the wing are very similar to the isolated surface pressures shown in Fig. 9. On the tail, however, the shock is weakened on the upper surface and the pressures near the lower surface leading edge are increased in magnitude due to the aerodynamically interfering wing. Also, the pressure distributions on the upper and lower tail surfaces are very similar which

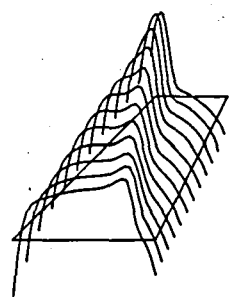

(a) upper surface.

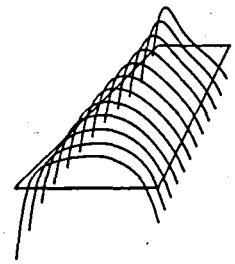

(b) lower surface.

Fig. 9 Steady pressure distributions on isolated lifting surface at M = 0.9 and α_0 = 2°;

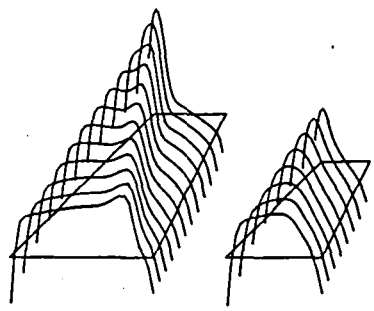

(a) upper surfaces.

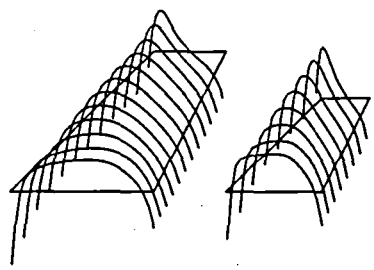

(b) lower surfaces.

Fig. 10 Steady pressure distributions on Laschka-Schmidt wing-tail at M = 0.9 and α_0 = 2° (S = 0.50);

indicates that the tail lift is small. Pressure distributions on the canard-wing upper and lower surfaces at M = 0.9 and α_0 = 2° are presented in Figs. 11(a) and 11(b), respectively. In general, the pressures on the wing resemble those of the isolated surface, although the lower surface values are slightly increased near the leading edge. On the canard, the upper surface shock is slightly weakened due to the presence of the wing. In contrast with the tail pressures of Fig. 10, the canard lifting pressure is of sizeable magnitude since the upper and lower surface pressure distributions are dissimilar.

To more clearly illustrate the steady transonic interaction between the two lifting surfaces, sectional lift coefficient distributions are presented in Figs. 12 and 13 for the wing-tail and canard-wing configurations, respectively. In each case, the horizontal separation distance is S = 0.5. Results for the isolated lifting surface (solid lines) are also plotted for comparison purposes. For the wing-tail configuration (Fig. 12), the tail induces a weak upwash on the wing which increases the wing sectional lift coefficient c_{ℓ_W} for all three angles of attack. Conversely, the wing induces a strong downwash on the tail which significantly reduces the tail sectional lift coefficient c_{ℓ_T}. Small negative values of c_{ℓ_T} result for the α_0 = 0° and 1° cases. Calculations for the closely-coupled wing-tail configuration (S = 0.25) resulted in negligible changes in c_{ℓ_W} and c_{ℓ_T} (not shown). For the

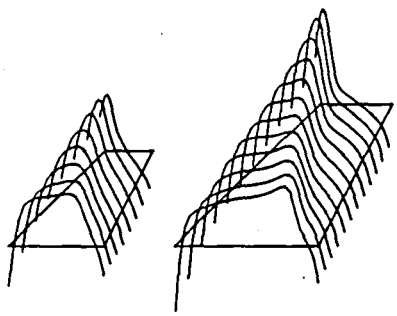

(a) upper surfaces.

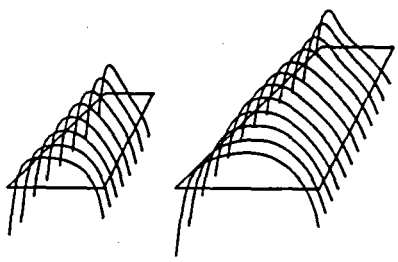

(b) lower surfaces.

Fig. 11 Steady pressure distributions on canard-wing configuration at M = 0.9 and α_0 = 2° (S = 0.50);

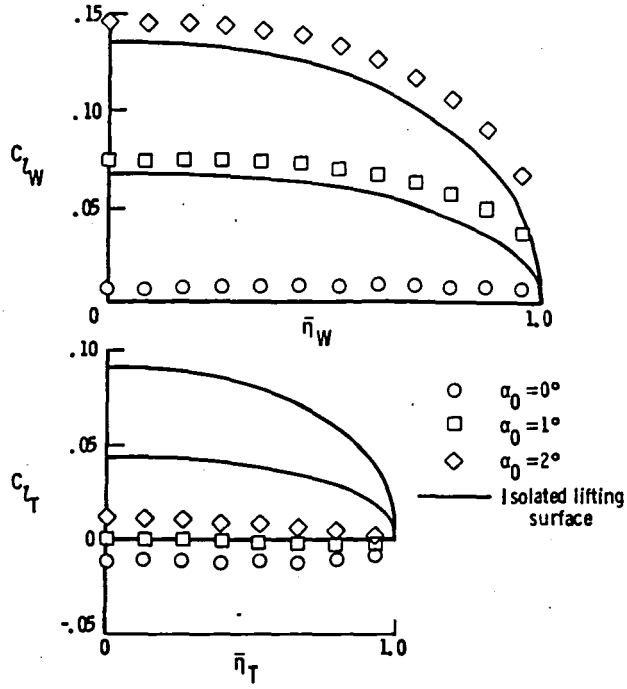

Fig. 12 Steady sectional lift coefficients on Laschka-Schmidt wing-tail at M = 0.9 (S = 0.50).

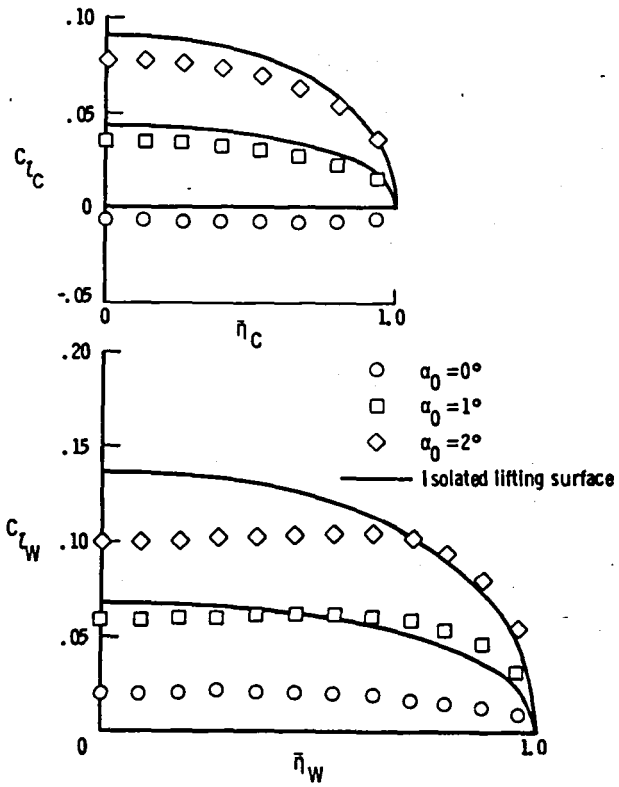

Fig. 13 Steady sectional lift coefficients on canard-wing configuration at M = 0.9 (S = 0.50).

canard-wing configuration (Fig. 13), the weak upstream influence of the wing slightly lowers the canard sectional lift coefficient c_{ℓ_C} at all three angles of attack. At $\alpha_0 = 0°$, the aerodynamically interfering canard induces a small positive spanwise lift distribution on the wing. As angle of attack is increased, the effect of the canard on the wing is increased, especially in the inboard region. At $\alpha_0 = 2°$, for example, the inboard wing lift is significantly lowered by the canard downwash. The outboard wing lift is less affected by the presence of the canard, as expected. For the closely-coupled canard-wing configuration (S = 0.25), c_{ℓ_W} in the inboard region of the wing is further reduced with decreased separation distance (not shown).

Transonic Unsteady Interference Effects

Transonic unsteady calculations for the wing-tail and canard-wing configurations were performed for wing, tail, and canard pitching motions with oscillation amplitude $\alpha_i = 1°$. The freestream Mach number was M = 0.9, the mean angle of attack was $\alpha_0 = 2°$, and the reduced frequency was k = 0.3. The step size was chosen as $\Delta t = 0.01496$ which results in 700 time steps per cycle of motion. Calculations were performed for two different separation distances S = 0.25 and S = 0.50 to investigate the effects of separation distance on unsteady spanwise loadings. These calculations are compared with the isolated lifting surface pitching results to demonstrate the effects of unsteady aerodynamic interference.

Unsteady sectional lift coefficients for the wing-tail configuration are presented in Figs. 14 and 15 for wing pitching and tail pitching, respectively. As shown in the upper part of Fig. 14, the wing sectional lift coefficient due to wing pitching, termed self-induced wing lift, shows a small increase in the real part in comparison with the isolated lifting surface solution. The harmonic motion of the wing produces an oscillatory flow about the fixed tail. The resulting induced tail loading due to wing pitching is plotted in the lower part of Fig. 14. The tail sectional lift coefficients are of similar magnitude to the self-induced wing lift and are dependent upon the horizontal distance separating the two lifting surfaces. When the separation distance is reduced by a factor of two, the imaginary part of c_{ℓ_T} decreases and the magnitude of the real part increases. These changes in the real and imaginary parts occur such that the magnitude of c_{ℓ_T} is uneffected and the phase of c_{ℓ_T} is decreased with reduced separation distance S. The decreased phase of c_{ℓ_T} is physically related to the shorter time required for disturbances created by the wing to influence the tail. For tail pitching (Fig. 15), the tail spanwise loading shows only a small increase in both real and imaginary parts between the isolated lifting surface and wing-tail cases. The effect of the oscillating tail on the fixed wing is negligible even for the closely-coupled case of S = 0.25. This result may be attributed to the relatively long times associated with upstream propagating disturbances (from tail to wing) in comparison with downstream propagating disturbances (from

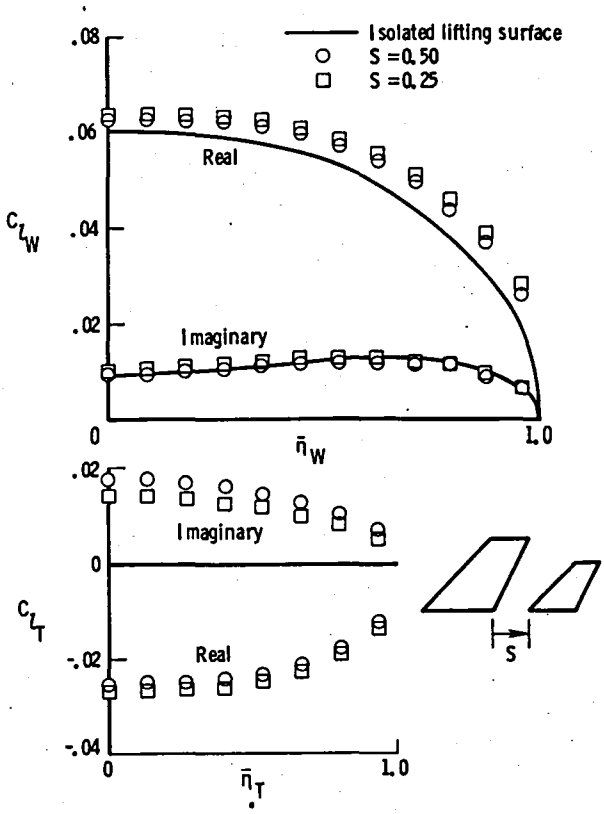

Fig. 14 Unsteady sectional lift coefficients on Laschka-Schmidt wing-tail due to wing pitching at M = 0.9, $\alpha_0 = 2°$, and k = 0.3.

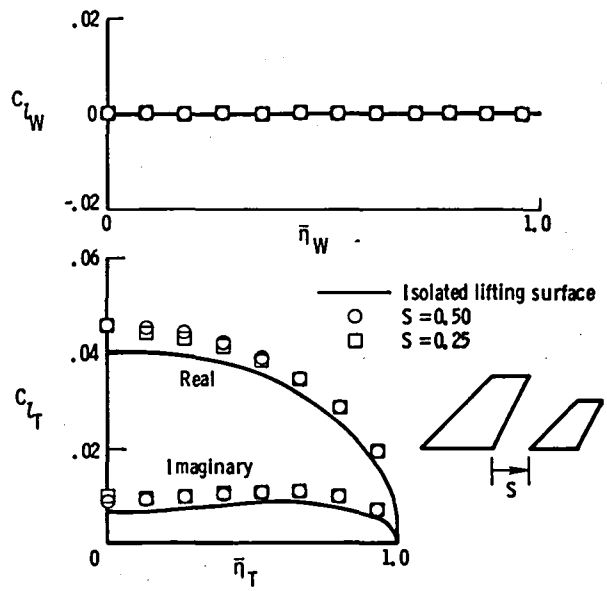

Fig. 15 Unsteady sectional lift coefficients on Laschka-Schmidt wing-tail due to tail pitching at M = 0.9, $\alpha_0 = 2°$, and k = 0.3.

wing to tail). For the freestream Mach number of M = 0.9 considered here, the downstream propagation speed is approximately nineteen times faster than the upstream propagation speed.

Unsteady sectional lift coefficients for the canard-wing configuration are presented in Figs. 16 and 17 for canard pitching and wing pitching, respectively. As shown in the upper part of Fig. 16, the canard sectional lift coefficient due to canard pitching, termed self-induced canard lift, shows only small differences between the isolated lifting surface and canard-wing cases. The harmonic motion of the canard produces an oscillatory flow about the wing. The resulting induced wing loading due to canard pitching is presented in the lower part of Fig. 16. The wing sectional lift coefficients are of similar magnitude to the self-induced canard sectional lift coefficients and are dependent upon the horizontal separation of the two lifting surfaces. With decreased separation distance, the magnitude of the wing sectional lift coefficients is slightly increased. The effect of the canard on the wing is largest in the inboard region and decreases outboard of the canard tip. For wing pitching (Fig. 17), the wing sectional lift coefficients show only very small increases in the real and imaginary components when the canard is included in the transonic flowfield. This negligibly small effect of the canard on the wing loading due to wing pitching is in contrast with the significant effect of the canard on the steady wing loading (Fig. 13). Similarly, the oscillating wing has no effect on the fixed canard for separation distances of S = 0.50 and 0.25 as shown in Fig. 17. This characteristic may be attributed to the relatively longer times for disturbances to propagate upstream from the oscillating wing to the motionless canard in comparison to downstream propagation from canard to wing as discussed previously for the wing-tail configuration.

Concluding Remarks

Steady and unsteady transonic flow calculations were presented for aerodynamically interfering lifting surface configurations. The calculations were performed by extending the XTRAN3S unsteady transonic small-disturbance code to allow the treatment of an additional lifting surface. The code is now capable of computing unsteady transonic flowfields about relatively general wing-tail and canard-wing configurations. Grid generation procedures for swept and tapered interfering lifting surface applications of XTRAN3S were described in detail. The planform finite-difference grid is based on the single surface grid mapping procedures which were extended to include an additional planform. Numerical instabilities at the root sections which were encountered in initial applications of XTRAN3S were eliminated using a new symmetric treatment of the grid across the reflection plane. Discontinuities in grid metrics were removed using an inboard grid mapping procedure with parabolic smoothing.

Unsteady subsonic calculations were performed for a simple wing-tail configuration

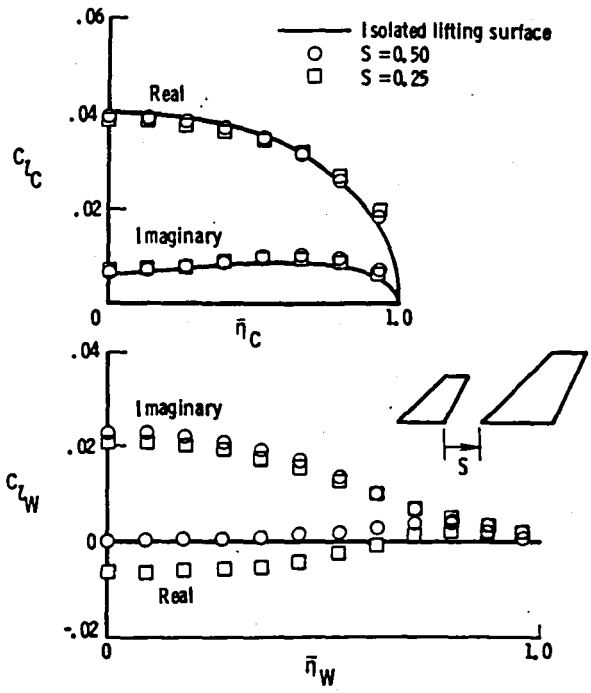

Fig. 16 Unsteady sectional lift coefficients on canard-wing configuration due to canard pitching at M = 0.9, α_0 = 2°, and k = 0.3.

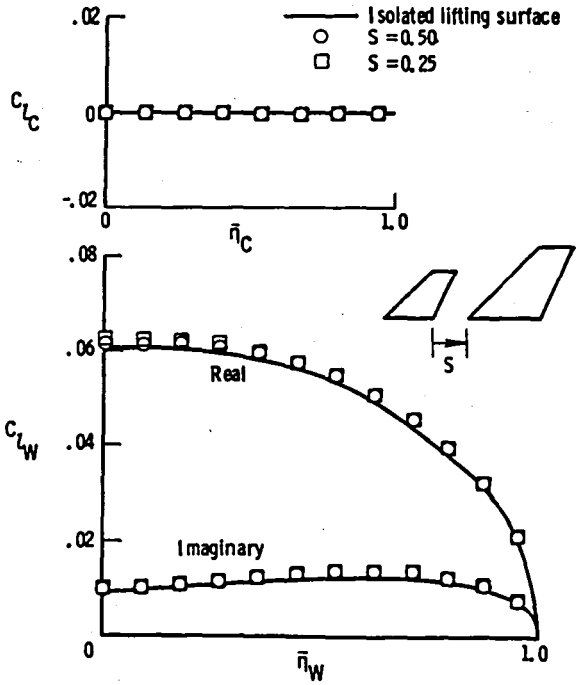

Fig. 17 Unsteady sectional lift coefficients on canard-wing configuration due to wing pitching at M = 0.9, α_0 = 2°, and k = 0.3.

consisting of two identical swept planforms to assess the modifications to the XTRAN3S code. Unsteady chordwise pressure distributions and spanwise lift distributions for wing pitching showed good agreement with published linear theory results. Steady transonic calculations were performed for swept and tapered wing-tail and canard-wing configurations at several mean angles of attack. The effects of aerodynamic interference were demonstrated on transonic steady pressure distributions and spanwise lift distributions. For the wing-tail configuration, the wing produced a downwash on the tail which significantly decreased the tail spanwise lift distribution. Conversely, the tail induced an upwash on the wing which increased the wing spanwise lift. For the canard-wing configuration, the canard produced a downwash on the wing which decreased the inboard wing spanwise lift at the higher angles of attack considered. The outboard wing lift was less affected by the presence of the canard, as expected. Unsteady transonic calculations were performed for wing, tail, or canard pitching motions. The effects of aerodynamic interference were demonstrated on transonic unsteady spanwise lift distributions. In general, the unsteady lift on one surface due to its own motion, termed self-induced lift, showed only small differences between isolated and interfering lifting surface cases. The induced lift on the aft surface due to motion of the forward surface, though, was dependent upon separation distance between the two lifting surfaces and was of similar magnitude to the self-induced lift. The effect of the oscillating aft surface on the forward surface was negligible.

The research was conducted as a first-step toward developing the capability to treat a complete flight vehicle. Transonic aeroelastic calculations are presently being performed for a closely-coupled canard and forward-swept wing configuration to investigate the effects of aerodynamic interference on stability and flutter. Work on developing a wing-body capability also is currently in progress.

References

[1]Proceedings of the AGARD Symposium on "Unsteady Aerodynamics for Aeroelastic Analyses of Interfering Surfaces", Tonsberg, Norway, November 3-4, 1970, AGARD-CP-80-71.

[2]Geising, J. P., Kalman, T. P., and Rodden, W. P., "Subsonic Unsteady Aerodynamics for General Configurations," AFFDL-TR-71-5, April, 1972.

[3]Laschka, B., and Schmidt, H., "Unsteady Aerodynamic Forces on Coplanar Lifting Surfaces in Subsonic Flow (Wing/Horizontal-Tail Interference)," Vereingte Flugtechnische Werke Gmbh Entwicklungs - Abteilung, Munchen, Report VFW M-72/66, December 1966.

[4]Albano, E., Perkinson, F., and Rodden, W. P., "Subsonic Lifting Surface Theory Aerodynamics and Flutter Analysis of Interfering Wing/Horizontal-Tail Configurations," AFFDL-TR-70-59, September 1970.

[5]Dusto, A. R., and Epton, M. A., "An Advanced Panel Method for Analysis of Arbitrary Configurations in Unsteady Subsonic Flow," NASA CR-152323, February 1980.

[6]Boppe, C. W., "Calculation of Transonic Wing Flows by Grid Embedding," AIAA Paper No. 77-207, presented at the AIAA 15th Aerospace Sciences Meeting, Los Angeles, CA, January 24-26, 1977.

[7]Shankar, V., and Malmuth, N. D., "Computational Treatment of Transonic Canard-Wing Interactions," AIAA Paper No. 82-0161, presented at the AIAA 20th Aerospace Sciences Meeting, Orlando, FL, January 11-14, 1982.

[8]Shankar, V., and Goebel, T., "A Numerical Transformation Solution Procedure for Closely-Coupled Canard-Wing Transonic Flows," AIAA Paper No. 83-0502, presented at the AIAA 21st Aerospace Sciences Meeting, Reno, NV, January 10-13, 1983.

[9]Shankar, V., and Goebel, T., "Treatment of Closely Coupled Canard-Wing Transonic Flows Including Dihedral," AIAA Paper No. 85-0428, presented at the AIAA 23rd Aerospace Sciences Meeting, Reno, NV, January 14-17, 1985.

[10]Batina, J. T., "Unsteady Transonic Flow Calculations for Two-Dimensional Canard-Wing Configurations with Aeroelastic Applications," AIAA Paper No. 85-0585, presented at the 26th AIAA/ASME/ASCE/AHS Structures, Structural Dynamics, and Materials Conference, Orlando, FL, April 15-17, 1985, also NASA TM 86375, February 1985.

[11]Whitlow, W., Jr., "XTRAN2L: A Program for Solving the General Frequency Unsteady Transonic Small Disturbance Equation," NASA TM 85723, November 1983.

[12]Borland, C. J., and Rizzetta, D. P., "Nonlinear Transonic Flutter Analysis," AIAA Journal, Vol. 20, No. 11, November, 1982, pp. 1606-1615.

[13]Borland, C. J., "Further Development of XTRAN3S Computer Program," NASA CR 172335, May 1984.

[14]Bennett, R. M., Seidel, D. A., and Sandford, M. C., "Transonic Calculations for a Flexible Supercritical Wing and Comparison with Experiment," AIAA Paper No. 85-0665, presented at the 26th AIAA/ASME/ASCE/AHS Structures, Structural Dynamics, and Materials Conference, Orlando, FL, April 15-17, 1985.

[15]Seidel, D. A., Bennett, R. M., and Whitlow, W., Jr., "An Explorating Study of Finite-Difference Grids for Transonic Unsteady Aerodynamics," AIAA Paper No. 83-0503, presented at the AIAA 21st Aerospace Sciences Meeting, Reno, NV, January 10-13, 1983.

[16]Stewart, V. R., "Evaluation of a Propulsive Wing/Canard Concept at Subsonic and Supersonic Speeds," Rockwell International Report NR82H-85, February 1983.

1. Report No.	2. Government Accession No.	3. Recipient's Catalog No.
NASA TM-86432		

4. Title and Subtitle	5. Report Date
UNSTEADY TRANSONIC FLOW CALCULATIONS FOR INTERFERING LIFTING SURFACE CONFIGURATIONS	May 1985
	6. Performing Organization Code: 505-33-43-09
7. Author(s): John T. Batina	8. Performing Organization Report No.
	10. Work Unit No.
9. Performing Organization Name and Address: NASA Langley Research Center, Hampton, VA 23665	11. Contract or Grant No.
	13. Type of Report and Period Covered: Technical memorandum
12. Sponsoring Agency Name and Address: National Aeronautics and Space Administration, Washington, DC 20546	14. Sponsoring Agency Code

15. Supplementary Notes

This paper will be presented at AIAA 18th Fluid Dynamics, Plasma Dynamics and Lasers Conference, Cincinnati, Ohio, July 16-18, 1985, as AIAA Paper No. 85-1711.

16. Abstract

Unsteady transonic flow calculations are presented for aerodynamically interfering lifting surface configurations. Calculations are performed by extending the XTRAN3S (Version 1.5) unsteady transonic small-disturbance code to allow the treatment of an additional lifting surface. The research was conducted as a first-step toward developing the capability to treat a complete flight vehicle. Grid generation procedures for swept tapered interfering lifting surface applications of XTRAN3S are described. Transonic calculations are presented for wing-tail and canard-wing configurations for several values of mean angle of attack. The effects of aerodynamic interference on transonic steady pressure distributions and steady and oscillatory spanwise lift distributions are demonstrated. Results due to wing, tail, or canard pitching motions are presented and discussed in detail.

17. Key Words (Suggested by Author(s))	18. Distribution Statement
Transonic Unsteady Aerodynamics Aerodynamic Interference Canard	Unclassified - Unlimited Subject Category 02

19. Security Classif. (of this report)	20. Security Classif. (of this page)	21. No. of Pages	22. Price
Unclassified	Unclassified	12	A02

For sale by the National Technical Information Service, Springfield, Virginia 22161

End of Document